Forced subduction initiation near spreading centers: effects of brittle-ductile damage

Mingqi Liu, Taras Gerya

Department of Earth Sciences, ETH Zurich, Sonneggstrasse 5, CH-8092 Zurich

Corresponding author: Mingqi Liu (mingqi.liu@erdw.ethz.ch)

Key Points:

- Upon forced compression, plates shorten, brittle parts thicken and new megathrust zone forms
- Strain-weakening of friction coefficient is crucial for the nucleation of new subduction zones
- Inherited detachment faults control lithospheric shortening but not subduction megathrust initiation

Abstract

Although positive buoyancy of young lithosphere near spreading centers does not favor subduction, subduction initiation near ridges may occur upon forced compression due to their intrinsic rheological weakness. It has been repeatedly proposed that detachment faults may directly control the nucleation of new subduction zones. However, recent 3D numerical experiments suggested that direct inversion of a single detachment fault does not occur. Here, we further investigate numerically this controversy by focussing on the influence of brittle-ductile damage on the dynamics of near-ridge subduction initiation. We model self-consistently the inversion of inherited long-term spreading patterns using 3D high-resolution thermomechanical numerical models combining strain weakening of faults with grain size evolution in lithospheric mantle. Numerical results show that development and evolution of detachment faults are strongly affected by the brittle-ductile damage coupling. Forced compression predominantly thickens the weakest near-ridge region of oceanic lithosphere, and reactivates inherited extensional faults. This results in rotation of blocks along reactivated faults leading to their subsequent locking. As the result, the development of a new megathrust zone occurs, which accommodates further shortening and subduction initiation. Strain weakening has a key impact on the collapse of thickening mid-ocean ridge region and the occurrence of near-ridge subduction initiation. In contrast, grain size evolution of mantle plays a subordinate role in these processes by slightly modifying the localization of shear zones near brittle-ductile transition. Through comparing with the geological record, our numerical results provide new helpful insights into natural near-ridge subduction initiation processes recorded by the Mirdita ophiolite of Albani.

Plain Language Summary

Intra-oceanic subduction, comprising 40% of the subduction margins, is widely distributed in the earth. It can bring oceanic slabs under the overriding parts of oceanic origin, forming oceanic magmatic arcs worldwide. Although several intra-oceanic subduction initiation models have been proposed, the question of how and where subduction initiates still remains elusive. Here, through 3D numerical models, we self-consistently explore the process of oceanic spreading followed by near-ridge subduction initiation and investigate the influence of brittle-ductile damage on this process. Numerical results demonstrate that plates shorten and thicken, and near-ridge faults rotate under forced compression, resulting in the newly formed megathrust zone and the subsequent near-ridge subduction initiation. Strain-weakening of friction coefficient is crucial for the collapse of thickening brittle layers. And thermal and compositional heterogeneities inherited from the seafloor spreading accommodate and control subduction angles and polarity. Furthermore, our model results provide new insights into the subduction initiation processes recorded by the Mirdita ophiolite of Albani.

1 Introduction

Subduction initiation and infancy remain controversial due to the limited observational constraints from the early stages of subduction (Stern and Gerya, 2018; Crameri et al., 2020; Lalemand and Arcay, 2021). Previous studies have categorized the subduction initiation into two modes - spontaneous and induced (Stern and Gerya, 2018) and proposed several tectonic settings such as (1) fracture zones or transform faults (Stern and Bloomer, 1992), (2) passive continental margins (Erickson, 1993; Regenauer-Lieb et al., 2001), (3) mantle plume (Gerya et al., 2015), (4) oceanic detachment faults (Maffione et al., 2015; Gulcher et al., 2019) and (5) oceanic spreading centers (Spray, 1983; Gurnis et al., 2004; Qing et al., 2021). However, despite the fact that oceanic spreading centers are some of the weakest parts of the Earth (Gurnis et al., 2004), the positive buoyancy of the young oceanic lithosphere presumably hampers the near-ridge subduction initiation. In particular, oceanic lithosphere should be at least 10 Myr old to become subductable due to own negative buoyancy compared to the ambient mantle (Cloose, 1993). In contrast, very young and

positively buoyant lithosphere near spreading centers can only start subducting by forced compression (Keenan et al., 2016). Paradoxically, under forced compression, near-ridge subduction can start considerably easier than the subduction of older an stronger oceanic lithosphere, which requires larger horizontal forces to cause the initial plate bending (Forsyth and Uyeda, 1975).

Young lithosphere with slow-ultraslow spreading rates deforms by slipping along large-offset detachment faults in large parts of the Atlantic, Indian, and Arctic Oceans (Dick et al., 2003; Cann et al., 1997; Escartn et al., 2008; Tucholke et al., 2008). Although lithosphere at fast-spreading ridges accretes through symmetric normal faults with relatively constant crustal thickness, it may also form detachment faults just prior to their termination due to the lowering of the spreading rate (Maffione et al., 2015). Lower crustal and mantle rocks are exhumed along detachment faults, forming dome-shaped structures at the seafloor (Garces and Gee, 2007; Morris et al., 2009; MacLeod et al., 2011; Sauter et al., 2013; Smith et al., 2008; Whitney et al., 2013). The rate of accretion of the oceanic crust varies dramatically, especially along ultraslow-slow spreading ridges, both in space and in time due to strongly fluctuating magma supply (Bown and White, 1994; Morgan and Chen, 1993; Liu et al., 2022). Studies from geophysical observations and numerical models indicated that the depth of detachment faults can reach 10-30 km, enhancing the hydrothermal circulation and alternation at spreading centers (e.g., Andreani et al., 2014; Bach et al., 2004, 2006; Beard et al., 2009; Bickert, et al., 2020; Boschi et al., 2006, 2013; Klein et al., 2009; Maffione et al., 2014; Mével, 2003; Plümper et al., 2012, 2014; Schroeder et al., 2002). At the root of detachment faults, especially at amagmatic sections, stain and stress concentrations lead to dynamic recrystallization, forming grain size reduction zones (Bickert et al., 2021). The combined effects of hydrothermal alteration and grain size reduction zones may further reduce near-ridge oceanic lithospheric strength and facilitate the stain location under compression, resulting in near-ridge subduction initiation along an inherited single detachment fault (Maffione et al., 2015).

Observations and computational simulations have both been used to investigate the subduction initiation by ridge inversion in the past (Gurnis et al., 2004; Keenan et al., 2016; Beaussier et al., 2019a, 2019b; Gulcher et al., 2019; Qing et al., 2021). Through comparing the oceanic crustal age with the overlaying lithospheric age and studying the timming of subduction intiation in the western Philippines, Keenan et al., (2016) found, at the time of subduction initiation, oceanic crust was less than 1 Myr old and implied that forced subduction initiated at a spreading ridge evolving from divergence to convergence. In 2D and 3D numerical models, effects of thermal states and geometries of spreading ridges were explored and numerical results indicated that warm paleo-ridge structures controlled by a short transition time from divergence to convergence favour the near-ridge subduction initiation (Gurnis et al., 2004; Beaussier et al., 2019a, 2019b; Qing et al., 2021). 2D models with a prescribed detachment fault suggested that ridge-inversed subduction may be directly controlled by the single detachment fault which reduces the lithospheric strength and enhances the strain localization (Maffione et al., 2015). However, recent 3D thermomechanical models suggested that the single detachment fault inversion is unlikely (Gulcher et al., 2019). Instead, the base of several inherited detachment faults become cut by newly formed subduction zone. Thus, the dynamic evolution and the rheological mechanisms of preexisting detachment faults formation and inversion remain controversial and require further numerical investigation.

Furthermore, the coupled brittle-ductile damage induced by strain weakening of faults and grain damage in the lithosphere (e.g., Gerya et al., 2021) may be a critical potential mechanism to facilitate both detachment faults formation and subduction initiation by ridge inversion. Sufficient grain damage in the lithosphere promotes shear localization and long-lived weak zones, resulting in the accumulation of weak plate boundaries (Bercovici and Ricard, 2012, 2014). Spontaneous and accumulated brittle-ductile damage caused by lateral stress may facilitate passive margins collapse

(Bercovici and Mulyukova, 2021). Previous numerical models with grain size evolution suggested that grain size reduction can produce weakening in the ductile regime, which leads to sufficient localization to trigger an oceanic transform fault (Schierjott et al., 2020). And brittle-damage damage localization in the subduction zone can produce pervasive subducting slab weakening and dynamic slab segmentation (Gerya et al., 2021). However the effect of brittle-ductile damage on ridge-inversed subduction initiation has never been investigated numerically, which gives further motivation for performing systematic numerical modeling.

In this paper, we focus on the influence of brittle-ductile damage on both the detachment faults formation and the subsequent ridge-inversed subduction initiation. We model the spontaneous formation and inversion of inherited spreading patterns after long spreading through 3D high-resolution thermomechanical numerical modeling combining strain weakening of faults with grain growth and grain damage in the mantle lithosphere. The intensity of strain weakening, grain damage, mantle potential temperature, and convergence rates are studied. And the influence of spreading rates and initial ridge geometries in the formation and inversion of detachment faults and transform faults are also explored. In addition, a new ridge-inversed subduction evolution process is proposed and compared with the recorded by the Mirdita ophiolite of Albani.

2 Methods and model setup

2.1 Numerical methods

Follwing Gerya, (2013) and Liu et al., (2022), we use 3D high-resolution thermomechanical numerical models which solve the incompressible mass, momentum, and heat conservation equation through the staggered finite differences method and marker-in-cell techniques (Gerya and Yuen, 2007). Brittle/plastic and viscous deformation mechanisms are implemented through the effective viscosity in this study. The strain-dependent Drucker-Prager criterion is used in the brittle/plastic part to simulate the fracture-related strain weakening:

$$\eta_{plastic} = \frac{\sigma_{yield}}{2\dot{\varepsilon_{II}}}, (1)$$

$$\sigma_{yield} = C_\gamma + \varphi(P - P_f), (2)$$

Where $\eta_{plastic}$ is the effective plastic viscosity, σ_{yield} is the scalar yield stress, and $\dot{\varepsilon_{II}}$ is the second invariant of the strain rate tensor. C_γ is the cohesion, P is the total pressure in the solid matrix, and P_f is the hydrostatic fluid pressure. φ is the internal friction coefficient which is controlled by the plastic strain γ (time-integrating the second invariant of the plastic strain rate tensor $\dot{\varepsilon}_{ij(\mathrm{plastic})}$) through the linear interpolation:

$$\varphi = 1, when\ P < P_f\ (tensile\ fracture)), (3a)$$

$$\left.\begin{array}{l} \varphi = \varphi_0, for\ \gamma \le \gamma_0 \\ \varphi = \varphi_0 + (\gamma - \gamma_0)\dfrac{\varphi_1 - \varphi_0}{\gamma_1 - \gamma_0}, for\ \gamma_0 < \gamma \le \gamma_1 \\ \varphi = \varphi_1, for\ \gamma > \gamma_1 \end{array}\right\}, when\ P \ge P_f\ (confined\ fracture), (3b)$$

Where φ_0 and $\varphi_1$are the upper and lower limits of friction coefficient, respectively.

Following Liu et al., (2022), in the ductile part, the effective ductile viscosity following a composite law is calculated by harmonic averaging of both dislocation and diffusion creep mechanisms. A constant grain size is used in the crustal material, while the process of both grain growth and grain damage are implemented in the mantle rocks. The dominant rheology is calculated through viscosity ratios of both dislocation and diffusion creeps. Final effective viscosity is a combination of plastic and ductile rheology and defined as the minimum value:

$\eta_{eff} = \min(\eta_{plastic}, \eta_{ductile})$. More details about numerical method and grain size evolution can be obtained from the Supporting information and and Liu et al., (2022).

2.2 Model setup

As shown in Fig. 1, the model domain is defined as a box of 202 × 98 × 202 km with 0.5 km high grid resolution in each direction and around 130 million randomly distributed Lagrangian markers. We set symmetrical oceanic plates (0.1 Myr in the center and 10 Myr at both left and right boundaries) with 7-km thick oceanic crust along x direction to mimic the incipient oceanic spreading. The half-space cooling model with constant thermal diffusivity (Turcotte and Schubert, 2002) is used to implement the initial thermal configuration. Constant temperatures are implemented at the upper and lower boundaries. To simulate various mantle potential temperatures, different temperatures are implemented at the lower boundary (Liu et al., 2022). Spreading/convergent rates are implemented at left and right boundaries along x direction ($v_{spreading} = v_{left} + v_{right}$, and $v_{left} = v_{right}$). To ensure the mass conservation in the computational domain, we set the compensating velocities at the upper (for the sticky air and water layer) and lower (for mantle rocks) boundaries along y direction. The transition from extension to compression is calculated by linear interpolation (Fig. 1c). The duration of the transition scales with the initially imposed spreading rate to ensure a constant rate of plate velocity change. Upon forced compression, subduction initiation occurs at or near the spreading center.

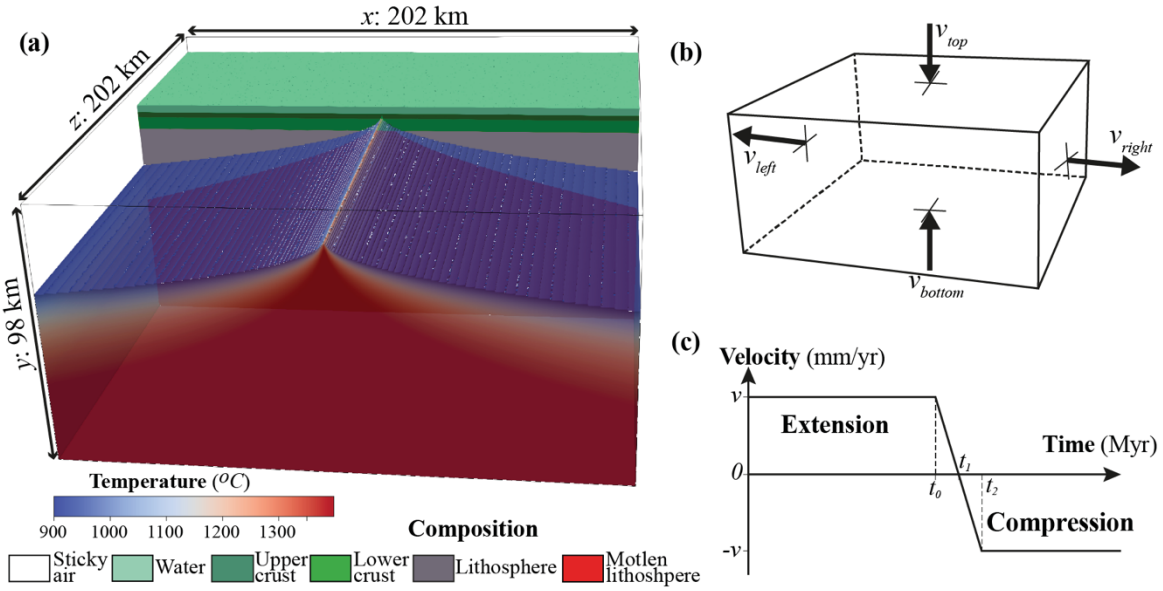

Figure 1. Initial model setup and boundary conditions. Composition and thermal configurations. Sticky air and water are implemented at the top boundary to simulate the topography. (b) Boundary conditions are lateral inflow/outflow in x direction and compensating through vertical influx velocities in y direction (v_{top} and v_{bottom}). (c) Prescribed lateral velocity boundary conditions. Transition ($t_0 - t_2$) from extension to compression is computed by linear interpolation. 0 mm/yr is at t_1.

3 Numerical results

23 numerical models are run to systematically investigate the influence of brittle-ductile damage on the near-ridge subduction initiation by modeling the inversion of inherited spreading patterns after long spreading (Table 1). Spreading rates, mantle potential temperature, convergence

rates, ridge geometries, and brittle-ductile damage are explored in these models. Representative numerical results are discussed below.

3.1 Reference model development from divergence to convergence

The reference model is implemented with the ultraslow spreading rate (10 mm/yr) and constant mantle potential temperature (1340^{o}C) to simulate the formation of detachment faults and explore the effect of brittle-ductile damage in the ridge-inversed subduction initiation. The interval from divergence to convergence is set to 3Myr (12 -15 Myr) to ensure a smooth transition. Numerical results at both divergence and convergence stages are presented in Fig. 2. Over 12 Myr of oceanic spreading, fundamentally different magmatic and amagmatic ridge sections (Liu et al., 2022) with long-lived detachment faults form spontaneously and alternate along the spreading ridge (Fig. 2a). Hot and thin brittle/plastic layer are produced in magmatic sections with elevated topography and normal thickness of oceanic crust (Fig. 2a, 3a), while mantle-derived rocks with grain damage are exhumated into the seafloor in amagmatic ridge sections with lowered topography, cold and thick brittle/plastic layer (Fig. 2a, 3b). Grain damage occurs at the root of the detachment fault and weakens the rheological strength in which deformation is dominated by grain size sensitive diffusion creep (Fig. 3), especially in amagmatic sections. In contrast with oblique spreading ridges in wide amagmatic sections (Fig. 2a), narrow and weak fracture zone with grain damage leads to a large offset between adjacent magmatic spreading ridge segments. After the transition to convergence (from 13.5 Myr), inherited detachment faults near spreading centers are reactivated, resulting in shortening of former spreading ridges, thickening of brittle layer, and rotation of inherited blocks(Fig. 3). Under the continued compression, gradual cooling and/or grain damage lead to the narrow weak region with smaller grain size beneath the former spreading ridge (Fig. 3 at 13.9 Myr), and then strain localization induced by the rotation goes deeply along this narrow weak region with further and deeper grain size reduction in the mantle (Fig. 3 at 15 Myr). Subduction initiates along the newly generated strain localization zone once movements of tectonic blocks near the former spreading centers become arrested within the relatively uniform thickened brittle/plastic lithospheric layer (Fig. 3 at 15-16 Myr). A pronounced subduction thrust forms at 17 Myr (Figs. 2b and 3) with a trench located 20-40 km away from the former spreading center.

Brittle-ductile damage thus plays significant role for both the inversion of inherited spreading patterns by lithospheric shortening and subsequent subduction initiation. Due to narrower weak regions and more uniform thickness of the brittle layer in cold amagmatic sections compared to hot magmatic sections, subduction initiates earlier in amagmatic sections than in magmatic ones (cf. Fig. 3b and 3a). Furthermore, different spreading configurations inherited from divergence in each section cause different geometries, resulting in variable subduction angles (Fig. 2b). Brittle-ductile damage in amagmatic sections helps creating initial curved subduction megathrust interface (Fig. 2b).

Focusing on the evolution of the reference model (Fig. 3), we can see that inherited detachment faults formed during divergence are not able to directly control the subduction initiation. Under convergence, inherited faults are reactivated and lead to the rotation of blocks within shortening and thickening spreading ridges. As the result, inherited low-angle faults rotate toward unfavorable steep/vertical angles which lead to their gradual locking and strain localization along the newly formed shallower angle thrust zone. Therefore, inherited brittle-ductile damage along detachment faults controls lithospheric shortening rather than subduction megathrust initiation.

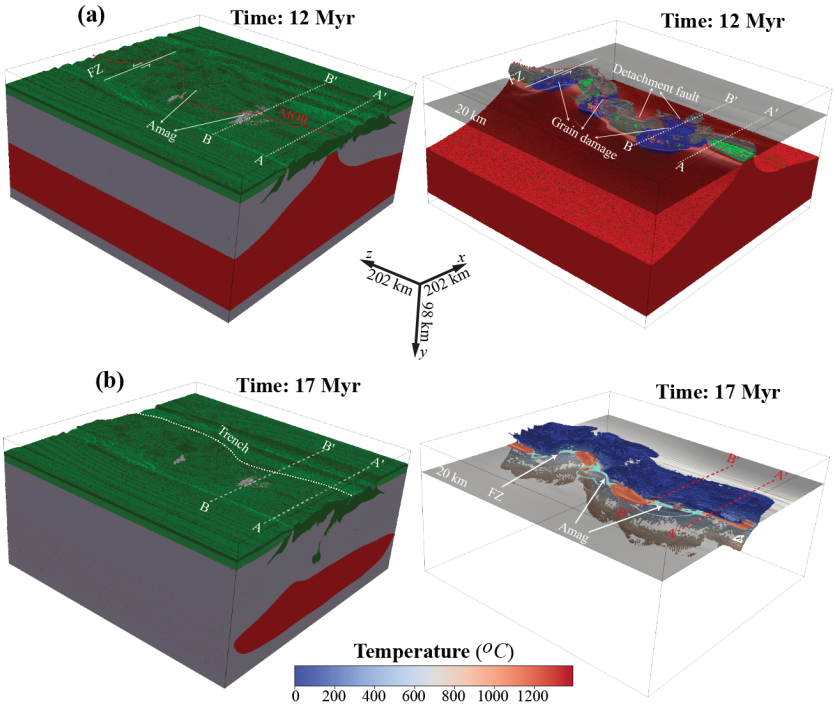

Figure 2. Reference model results at both of divergence and convergence stages. Distribution of composition (left) and detachment faults along the ridge (right) at 12 Myr which is the start of transition from divergence (a) to convergence (b). (a) Rock types distribution (left) and ridge structure (right) at 12 Myr when the oceanic spreading ends. The dashed red line shows the location of spreading ridges. Grain damage is present in amagmatic sections (Amg) and fracture zones (FZ) with blue color in the right panel. Newly formed oceanic crust without grain size evolution is shown by grey color in the magmatic sections. (b) Composition distribution (left) and subduction slab (right) at 17 Myr when the subduction megathrust formed. The dashed white line marks the subduction trench. Subduction slab with thermal distribution is extracted through the high strain rate, $> 5e-14\,s^{-1}$. Grain damage (light green) and high strain localization (orange) along spreading centers in the horizontal depth of 20 km at the end of divergence are presented. The translucent plane of the second strain rate invariant at the depth of 20 km at 17 Myr are shown in rights panels of (a) and (b). Dashed lines A-A' and B-B' mark locations of vertical profiles in Fig. 3.

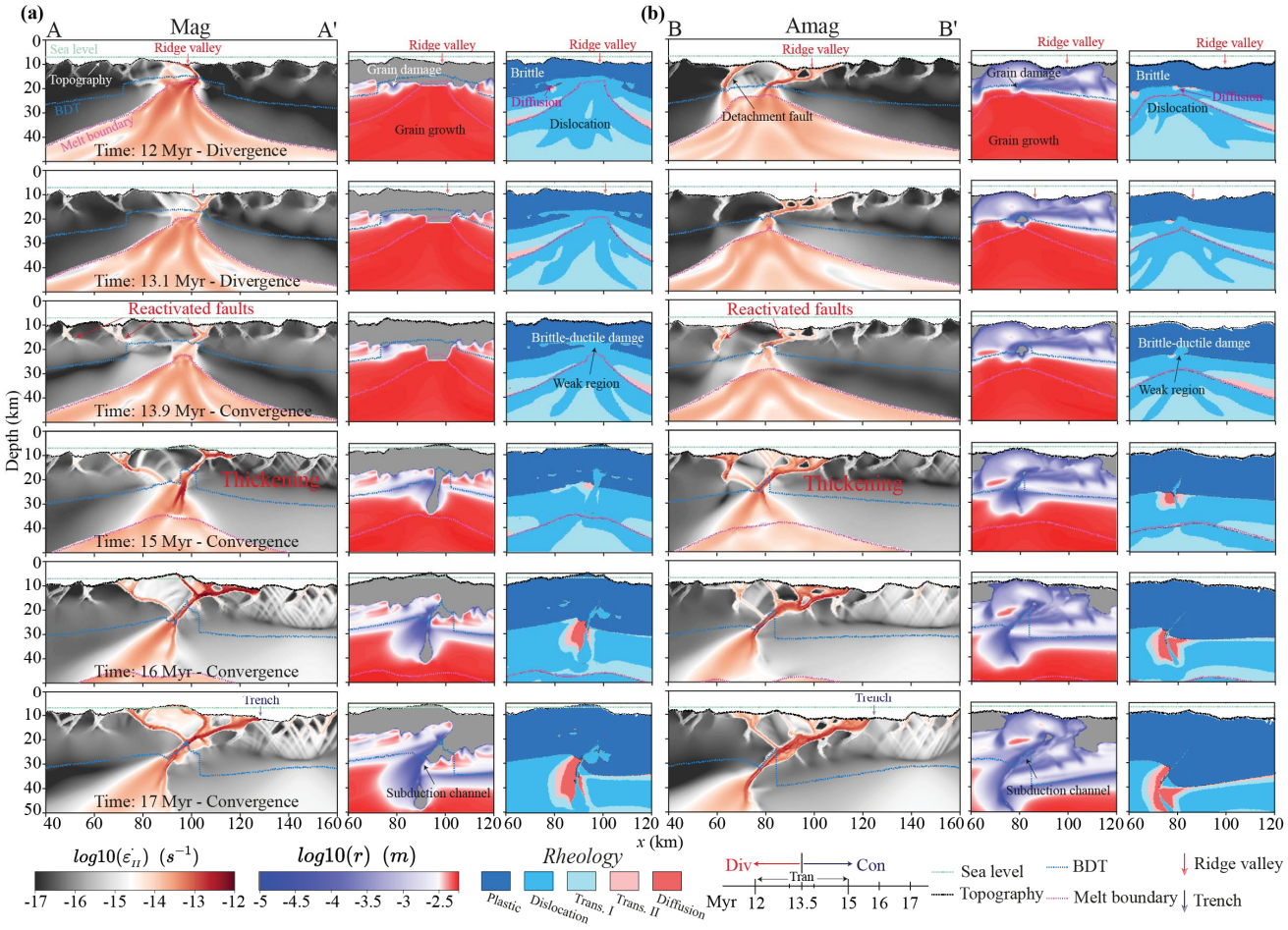

Figure 3. Evolution of the reference model from divergence to convergence.
(a) Profiles along $A - A'$ at the magmatic section. (b) Profiles along $B - B'$ at the amagmatic section. The second invariant of strain rate, grain size, and rheological mechanism are presented from left to right. Locations of profiles are marked in Fig. 2. Div, divergence. Con, convergence. Tran, transition. BDT, brittle-ductile transition.

3.2 Influence of strain weakening and grain damage

Previous studies have proved that various weakening mechanisms have a significant impact on both oceanic spreading patterns and ridge-inversed subduction initiation (Keenan et al., 2016; Gulcher et al., 2019; Beaussier et al., 2019a, 2019b; Qing et al., 2021; Liu et al., 2022). Here, we explore the effects of two main weakening mechanisms: strain-dependent friction coefficient weakening to localize deformation and grain damage by dynamic recrystallization.

Models with varying strain weakening intensities and grain damage are shown in Fig. 4. In the model with strong strain weakening ($\varphi_1 = 0$) and grain damage, strongly curved spreading ridges at the end of divergence are prominent, which indicates a greater weakening of fractured rocks and a larger offset of detachment faults. Magmatic and amagmatic sections alternate with the almost same length. Under compression, detachment faults near spreading centers are reactivated and then rotated, resulting in the newly formed strain localization. The ridge-inversed subduction initiates towards the spreading centers along the new weak zone. With the decreasing of strain weakening intensity (increasing φ_1), smaller strain weakening intensity results in a smaller offset of detachment faults and much straighter spreading ridges. And amagmatic sections become much sparser and narrower. The model with only grain size evolution as the sole weakening mechanism develops

conjugate faults, rooting into the brittle-duction transition (Fig. 5). The intersection of both conjugate faults reaches below the seafloor at the end of divergence, forming the axial rift. The spreading pattern with conjugated faults is obviously different from the spreading pattern in the reference model which develops long-lived large offset detachment faults. Upon forced compression, conjugate thrusts form at former spreading centers in models with smaller strain weakening intensity. Continued compression is mainly accommodated by shortening of the swelling ridges with high topography till its collapse in these models. Yet, due to extremely small strain weakening intensity in models with the largest φ_1 (0.6), the swelling ridges are difficult to collapse and fail to develop subduction initiation.

In contrast to strain weakening, the effects of grain damage are relatively small for both the formation of spreading patterns and the ridge-inversed subduction initiation. In models with strong strain weakening ($\varphi_1 = 0$), curved spreading ridges are observed both with and without grain damage. Alternate magmatic and amagmatic sections are also documented in both types of models and ridge-inversed subduction initiates toward spreading ridges along the newly formed weak thrusting zone. Subduction angles are accommodated by amagmatic sections. Especially, narrow fracture zones with large offset lead to the rapid transition of subduction angles (Fig. 2) or opposite subduction polarity (Fig. 4), which may be mainly controlled by the shortening and rotation of faults near former spreading ridges. In models with small strain weakening intensity ($\varphi_1 \leq 0.3$), regardless of grain damage, spreading ridges are always straight and swelling ridges form under compression. However, due to the grain damage at roots of detachment faults in amagmatic sections and brittle-ductile transition (Fig. 5), the weak mantle is prone to swell instead of collapse under compression. Therefore, the stronger swelling ridges in models without grain damage are easier to collapse and develop the subduction initiation (Fig. 4).

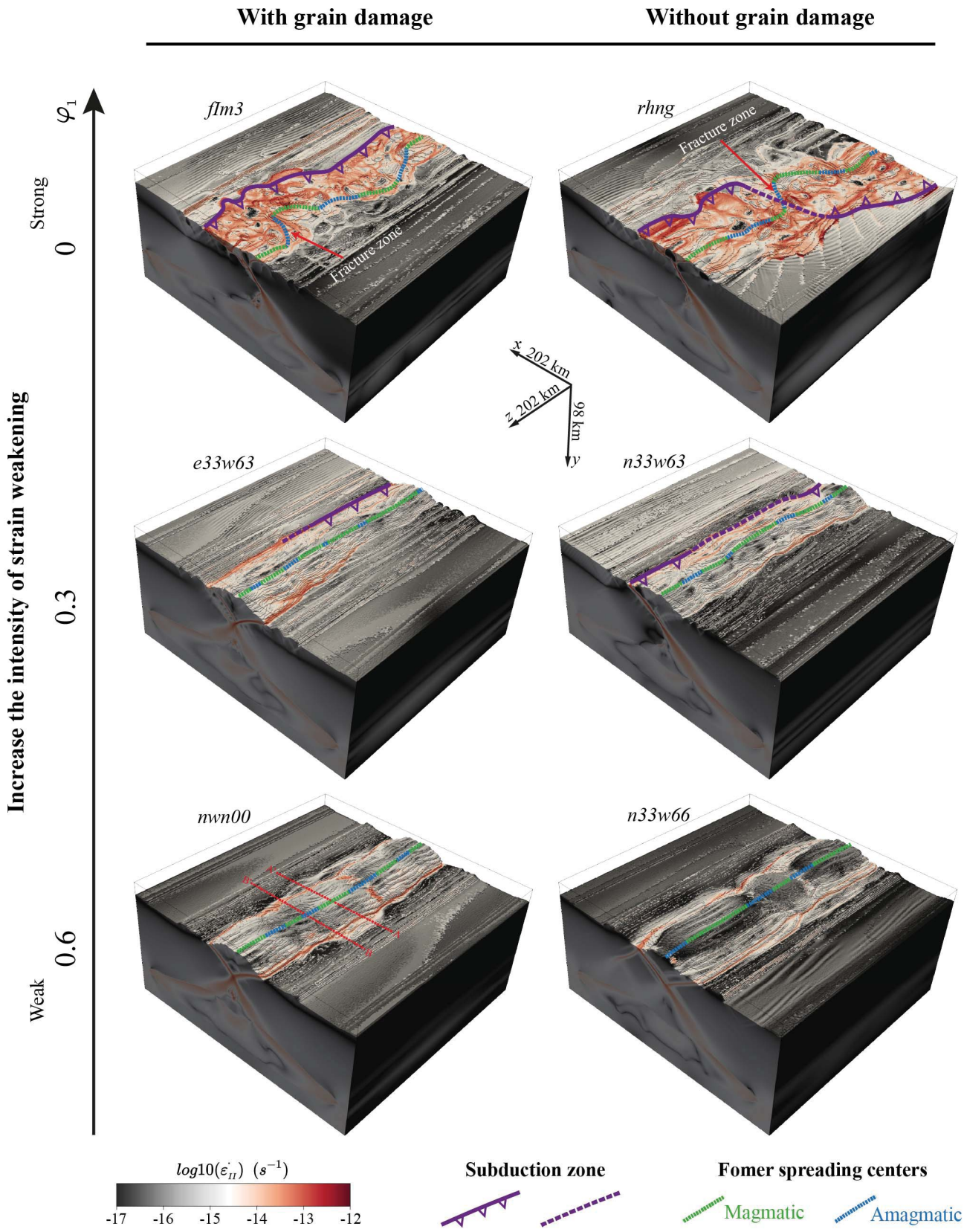

Figure 4. Effects of strain weakening intensities and grain damage in the ridge-inversed subdcution.

Former spreading centers are presented in green (magmatic segments) and blue (amagmatic segments) dashed lines. Subduction zones are indicated through purple lines with triangles. Dashed

purple lines mark the transition. Red dashed lines in the model of nwn00 mark locations of vertical profiles in Fig 5.

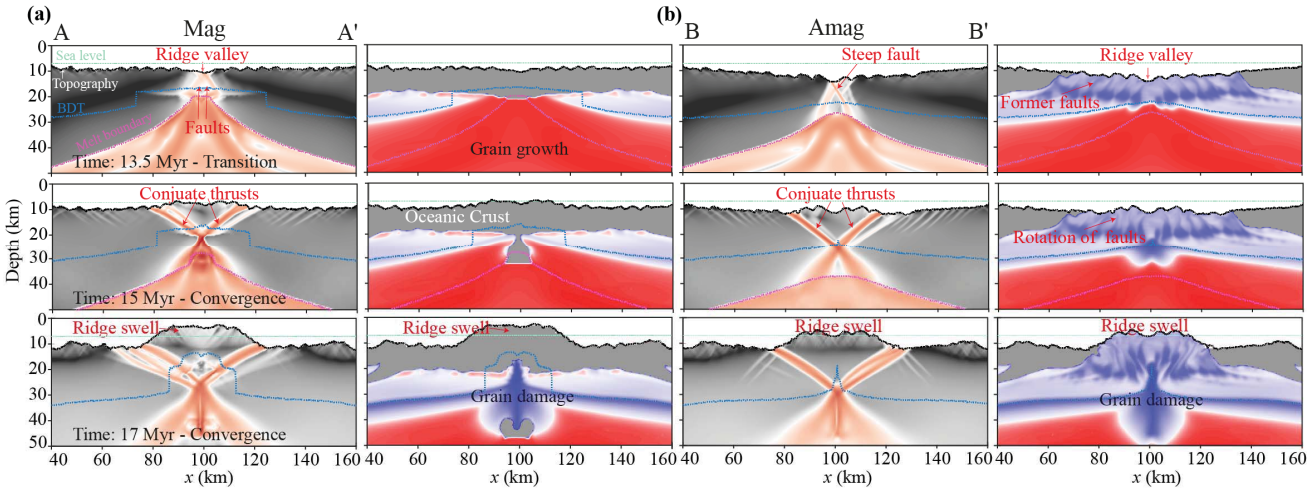

Figure 5. Ridge-inversion results of the model, *nwn00*, without strain weakening. (a) Profiles along $A - A'$ at the magmatic section. (b) Profiles along $B - B'$ at the amagmatic section. The second invariant of strain rate and grain damage are presented from left to right. Locations of profiles are marked in Fig. 4. Color codes are the same with Fig. 3.

3.3 Influence of variable mantle potential temperature

The effects of increasing/decreasing mantle potential temperature are explored (Fig. 6). The most obvious difference between these models is the temperature configuration and the magma supply beneath spreading centers which significantly influence the distribution of magmatic and amagmatic sections along spreading ridges and subsequent ridge-inversed subduction initiation.

During divergence, high potential temperature leads to hot thermal configuration and a great amount of magma supply, resulting in the only formation of the magmatic section with thick oceanic crust and grain growth in the mantle. Owing to the hot and weak mantle, very large offset (over 100 km) detachment faults with rolling-hinge mode form and transform faults develop (Fig. 6a). Yet, cold thermal structure in the model with low mantle potential temperature produces a small magma supply and causes thick brittle lithospheric layer, resulting in only several small magmatic sections observed (Fig. 6c). Under compression, when compared to the reference model, due to the weaker mantle in the model with high potential temperature, reactivated faults near spreading centers slightly rotate, and then subduction initiates along the reactivated fault which is far away from the spreading center. However, in the low mantle potential temperature, after shortening and thickening, the newly formed weak zone is opposite with former and near-ridge detachment fault. Grain damage along the new weak zone facilitates the subduction initiation. Furthermore, according to locations of narrow fracture zones and opposite subduction polarity, the presence of inherited narrow fracture zones with large offset are a potential mechanism to trigger the development of opposite subduction polarity.

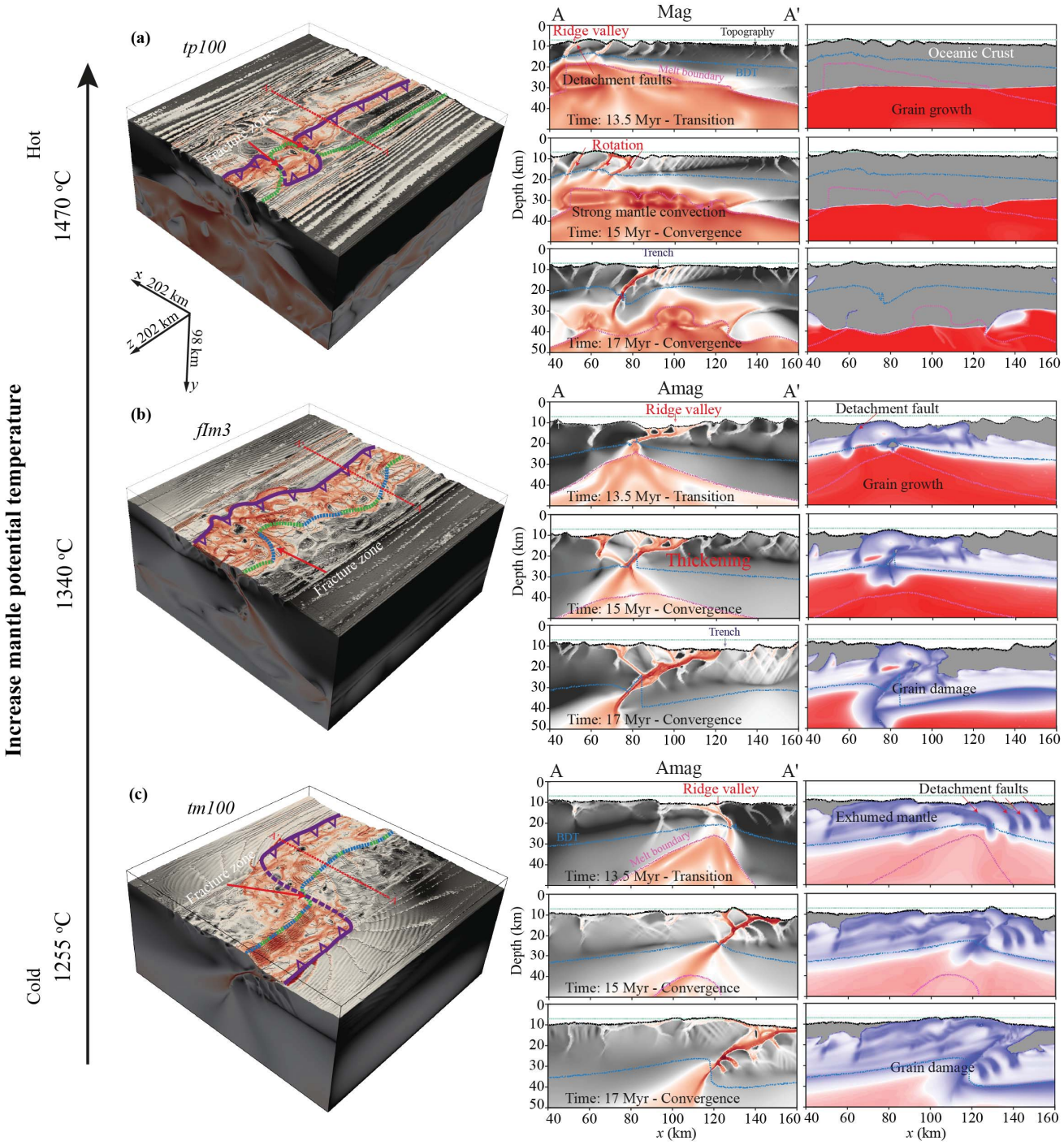

Figure 6. Ridge-inversed subduction with variable mantle potential temperatures. (a-c) Left panel: Ridge-inversed subduction results with variable mantle temperatures; right panels: results of evolution along the red line in the left panel. Strain rate and grain size distribution are displayed. The color codes are the same with Figs. 3 and 4.

3.4 Influence of variable convergence rates

Previous studies have suggested that convergence rates have a significant impact on the rheological coupling between plates (Faccenda et al., 2008). Slow convergence rates cause strong rheological coupling between plates, while fast convergence rates lead to weak rheological coupling.

Therefore, we systematically investigated the effect of variable convergence rates in the formation of ridge-inversed subduction.

Divergence and convergence rates explored by different models are shown in Fig. 7(a). The spreading rates remained constant in these models whereas different convergence rates (and their different partitioning between the plates) are implemented during the convergence stage. In particular, variable convergence directions with the same full convergent rate (10 mm/yr) are implemented in models fIm3, continl, and continr. Half of the full rate is implemented in both left and right boundaries in model fIm3, while the full rate is prescribed in the left boundary in model continl and in the right boundary in model continr. Numerical results show that, at 17 Myr, except for the trench locations, subduction slabs share similar patterns in these three models (Fig. 7b) and are accommodated by amagmatic sections and fracture zones. In addition, variable convergence rates are implemented in models rheo1 (20 mm/yr), rheo2 (40 mm/yr), and rheo4 (80 mm/yr). As shown in Fig. 7(c), a low convergence rate (rheo1) causes the same subduction direction, while high convergence rates (40 and 80 mm/yr) induce opposite subduction polarity. This may indicate that convergence rates play a significant role in the rheological couping during the shortening, thickening, and rotation of inherited detachment faults. Regardless of convergence partitioning between plates, the same convergence rates always develop similar subduction initiation patterns. However, variable convergence rates may change the convergent process, brittle-ductile damage, and the rheological coupling conditions, which further leads to different newly formed lithospheric strain localization pattern. Subduction initiates along the new weak shear zones and forms opposite subduction polarity in different ridge sections.

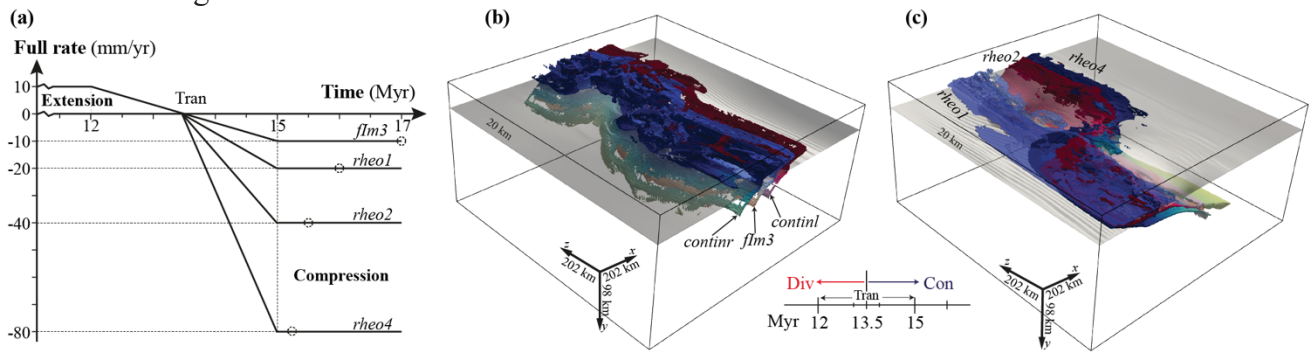

Figure 7. Ridge-inversed subduction initiation results from different convergence rates. Prescribed lateral velocity boundary conditions. (b) Ridge-inversed subduction results with variable convergence directions. (c) Ridge-inversed subduction results with variable convergence rates. Convergence lengths in all models are almost the same, about 30 km.

4 Discussion

Due to the positive buoyancy at young spreading ridges, ridge-inversed subduction initiation has been considered difficult until recently. Although many numerical models have investigated its mechanisms and processes (Gurnis et al., 2004; Maffione et al., 2015; Keenan et al., 2016; Beaussier et al., 2019a, 2019b; Gulcher et al., 2019; Qing et al., 2021), this mechanism still remain partly elusive. Through 3D high-resolution self-consistent magmatic-thermomechanical numerical models, we find that tectonic patterns inherited from seafloor spreading and new weak shear zones formed after shortening, thickening, and rotation of former detachment faults near spreading centers upon forced compression (Fig. 8) have a great impact on the ridge-inversed subduction initiation. In addition, thermal and compositional heterogeneities from magmatic and amagmatic sections and transform faults accommodate and control subduction angles and polarity.

4.1 Near-ridge lithospheric stain localization under compression

In our models, detachment fault can be formed not only in slow-ultraslow spreading rates but also at the terminal stage of spreading in intermediate spreading models (Table 1). Previous studies have proposed that near-ridge subduction initiation is directly controlled by the single detachment fault (Maffione et al., 2015) or the nascent subduction zone cuts through the base of previous detachment faults (Gulcher et al., 2019). Different from these studies, through systematic numerical models, we find that the ridge-inversed subduction initiation goes through three main stages (Fig. 8): (1) inherited tectonic pattern from seafloor spreading. It may include thermal and compositional heterogeneities, geometries of spreading ridges, faults orientations, transform faults, et al. (2) Shortening and thickening of spreading ridges. Under compression, spreading ridges are gradually shortening and thickening, resulting in relatively uniform brittle lithospheric layer in both plates and the rotation of near-ridge faults and blocks. Afterward, the newly formed strain localization goes deeply through the narrow weak region. (3) Subduction initiates along the newly formed strain localization zone towards former spreading ridges. Subduction angles are accommodated by the inherited tectonic patterns. Opposite subduction polarity may occur, which is triggered by inherited transform faults. In addition, along spreading ridges, owing to brittle-ductile damage, the earlier strain localization in wide amagmatic sections promotes the strain localization in adjacent magmatic sections.

Effects of weakening mechanisms show that strain-dependent friction coefficient weakening plays an essential role in ridge-inversed subduction initiation. Model without strain weakening (Fig. 4) forms conjugated large normal faults in the terminal stage of spreading. Under forced compression, symmetric conjugated thrusts cause high ridge swelling and fail to result in a subduction initiation, which is similar to model results with a high healing rate in Gulcher et al., (2019). Although Beaussier et al., (2019a, 2019b) proposed that the failure of ridge swelling from high gravitational potential energy under the continuous convergence leads to subduction initiation, our models suggest that strain-dependent friction coefficient weakening rather than high gravitational potential energy controls the occurrence of ridge-inversed subduction initiation. Ridge-inversed subduction initiates along the newly formed weak zone in models with strong strain weakening intensity, even if there is no swelling ridge (Fig. 4). However, if the intensity of strain weakening is extremely weak even though the ridge swelling is very high, subduction still fails to initiate. In addition, small effects of grain damage in the root region of detachment faults are observed which are consistent with the geological observation (Bickert et al., 2021). Compared to strain-dependent friction coefficient weakening, grain damage thus should only play a subordinate role in near-ridge lithospheric strain localization and subduction initiation.

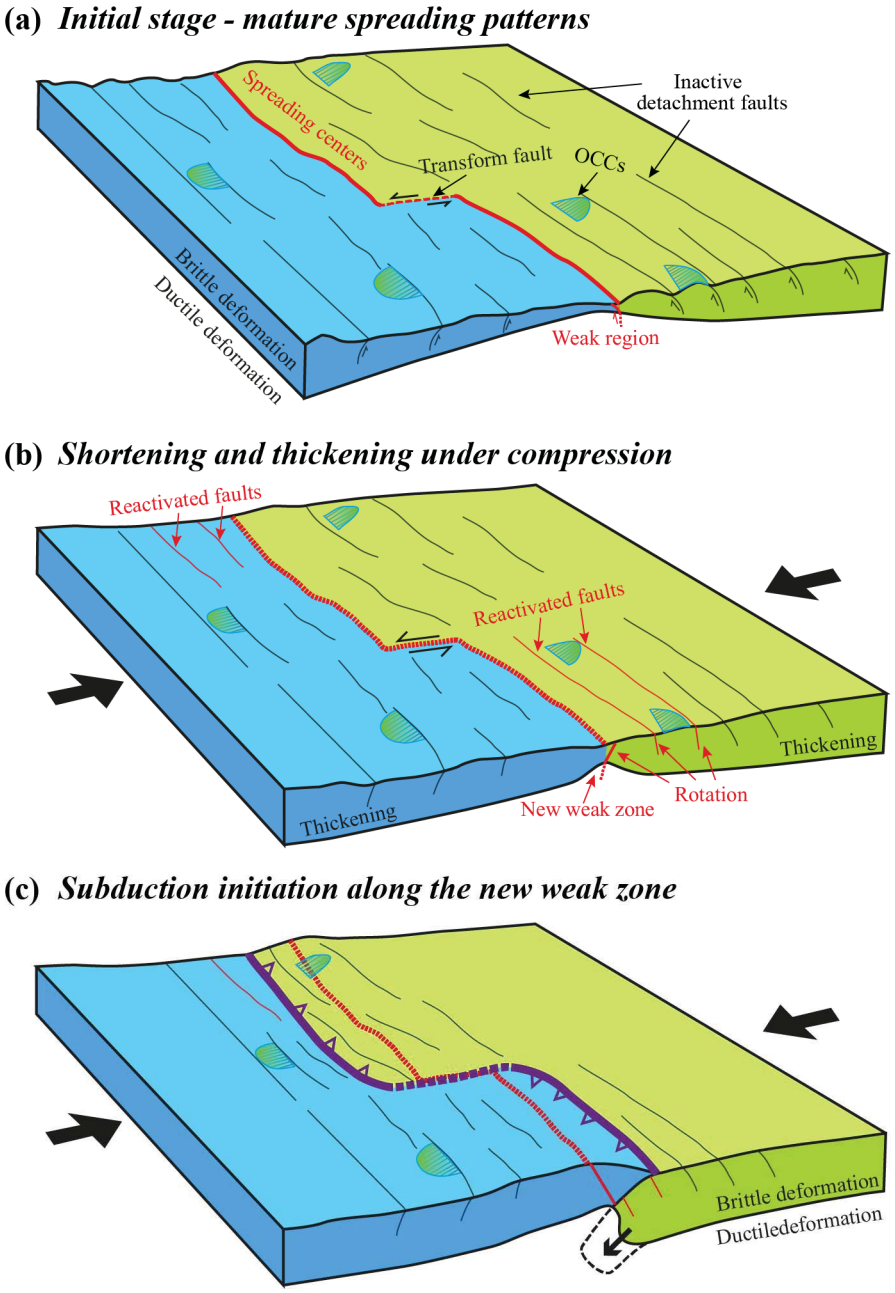

Figure 8. Schematic diagram of the ridge-inversed subduction evolution. Mature spreading patterns. Detachment faults formed under slow-ultraslow spreading rates exhume mantle rocks into the seafloor and yield oceanic core complexes (OCCs). (b) Oceanic pltaes shorten and thicken under compression. Faults near spreading ridges are reactivated and rotate, resulting in the newly formed weak zone. (c) Under continued compression, subduction initiates towards the former spreading centers along the newly formed weak zone. Transform faults or fracture zones may a potenital location to induce the opposite subduction polarity.

4.2 Effects of inherited tectonic spreading patterns in ridge-inversed subduction

Inherited heterogeneous tectonic patterns from seafloor spreading is crucial for the development of ridge-inversed subduction in our models. As found by Liu et al. (2022), spreading rates and mantle potential temperature are key controls for tectonic patterns along spreading centers. Small conjugate faults forming in symmetric spreading centers are induced by thin brittle/plastic

layer and intermediate-fast spreading rates. And deeply penetrating asymmetric detachment faults forming in thick brittle/plastic layer and amagmatic sections exhume mantle rocks and result in compositional heterogeneity along slow and ultraslow spreading ridges. High mantle potential temperature induces a high extent of mantle melting and sufficient magma supply, resulting in smooth bathymetry and uniformly thick oceanic crust along spreading ridges. In contrast, spare magmatic segments form at low potential temperature with three-dimensional heterogeneity along the spreading ridge due to insufficient magma supply. Furthermore, initial oblique spreading ridges can cause more magmatic and amagmatic sections and produce stepped ridge-transform patterns at the large oblique angle model (Table 1).

Inherited spreading patterns affect lithospheric strain localization and thereby control the near-ridge subduction angles under compression. Strain localization in cold wide amagmatic sections with deeply-rooted detachment faults and thick brittle layer forms earlier than that in magmatic sections with shallower detachment faults and thinner brittle layer. This in turn results in earlier subduction initiation in amagmatic sections, which in turn promotes subsequent subduction initiation in adjacent magmatic sections. Due to the composition and thermal differences between magmatic and amagmatic sections, shapes of subducting slabs are affected by the inherited ridge heterogeneity. In addition, mature transform faults with offset ridge sections are prone to induce opposite subduction polarity, which is consistent with previous studies (Beaussier et al., 2019a, 2019b). However, even the same inherited spreading pattern can still form different subduction polarities under different convergence rates. It is mainly because convergence rate magnitude can affect brittle-ductile damage and rheological coupling conditions (Faccenda et al., 2008), induce different strain localization, and form opposite subduction polarity (Qing et al., 2021). In contrast, the partitioning of convergence rate between the two plates does not produce any significant effect and results of experiments remain almost the same irrespective of convergence rate partitioning.

4.3 Comparison with previous numerical models

Ridge-inversed subduction initiation has been widely studied from geological observation to numerical models (Gurnis et al., 2004; Maffione et al., 2015; Keenan et al., 2016; Beaussier et al., 2019a, 2019b; Gulcher et al., 2019; Qing et al., 2021). For numerical models, 2D models with prescribed spreading ridge are set in Gurnis et al., (2004), Maffione et al., (2015), and Qing et al., (2021), while 3D models with inherited spreading patterns from continental rifting or spreading ridge are set in Beaussier et al., (2019a, 2019b) and Gulcher et al., (2019). In contrast with prescribed homogenous spreading ridges in 2D models, inherited spreading patterns evolving from continental rifting or spreading ridge in 3D models show thermal and compositional heterogeneities with variable geometries of spreading ridges. Forced subduction initiation in 2D models occurs along spreading ridges in the model with symmetric ridges (Gurnis et al., 2004; Qing et al., 2021) and along the detachment fault in the model with prescribed single detachment fault (Maffione et al., 2015). In 3D models with inherited spreading patterns, forced subduction initiation is mainly controlled by ridge swelling (Beaussier et al., 2019a, 2019b), while detachment faults are also observed and are cut by nascent subduction zones (Gulcher et al., 2019). Compared to recent 3D models (Beaussier et al., 2019a, 2019b; Gulcher et al., 2019), our models are set with higher resolution and bigger domain size as well as with coupled brittle-ductile damage (e.g., Gerya et al., 2021), which allows to more accurately resolve the transition from oceanic spreading to subduction initiation. The fine process from divergence to convergence shows that shorting and thickening of plates and the newly formed lithospheric strain localization are key factors of forced ridge-inversed subduction initiation in our models. Except for the hot and weak mantle in the high mantle potential temperature model, the direction of newly formed strain localization is independent of the orientation of the latest detachment fault formed during oceanic spreading stage. In addition, offset ridge

sections induced by spontaneously formed large offset transform faults are prone to form opposite subduction polarity.

4.4 Comparison with natural examples

Although many evolving processes are simplified in our models, it is essential to provide some helpful insights into the near-ridge subduction initiation. Occurrences of near-ridge subduction initiation around the world have been possibly recognized in the Mirdita ophiolite of Albania, the Proto-Palawan Trench, and the Yap trench (Fujiwara et al., 2000; Gurnis et al., 2004; Maffione et al., 2015; Keenan et al., 2016). The dynamics of ridge-inversed subduction have been widely discussed and compared with natural cases (Gurnis et al., 2004; Beaussier et al., 2019a, 2019b; Qing et al., 2021). Therefore, here we mainly focus on the effects of detachment faults in the newly formed strain localization, near-ridge subduction initiation, and the possible geological records in these cases.

Observations of the Jurassic ophiolites of Albania and Greece from geochemistry, structure geology, and paleomagnetism in Maffione et al., (2015) suggest that the subduction zone formed in the western Neotethys is parallel to the spreading ridges and related to the oceanic detachment faults. Similar ages between exposed mid-ocean ridge basalt (MORB) and supraduction zone (SSZ) indicate that no significant time gap exists between the pre-existing spreading centers and subduction initiation (Liati et al., 2004; Stern, 2004). Paleomagnetic constraints reveal that the preserved oceanic detachment faults and oceanic core complexes in the ultramafic Puka Massif (Maffione et al., 2013) are toward and close to the paleo-spreading ridges. Thus, forced convergence from the central Atlantic and the Alpine Tethys during the Middle Jurassic (Torsvik et al., 2012) may induce the subduction to initiate along detachments close to the spreading ridges rather than exactly at the spreading axis (Maffione et al., 2015). However, according to our 3D self-consistent thermomechanical numerical results (Fig. 2 and 3b), we find that upon forced convergence, weak pre-existing detachment faults are prone to thicken and rotate till locked up with high angles and then form new lithospheric strain localization instead of yielding the nucleation of new subduction zones along the fault planes. Finally, the subduction initiation starts along the newly formed shear zones rather than the detachment faults close to the spreading ridges.

5 Conclusion

3D high-resolution self-consistent thermomechanical numerical models with brittle-ductile damage are conducted to study the forced near-ridge subduction initiation by modeling the inversion of inherited mature spreading patterns formed after long-term spreading. Our model results suggest that upon compression, plates shorten and thicken and inherited near-ridge faults rotate, resulting in the newly formed lithospheric strain localization along the emerging megathrust. Subsequently, near-ridge subduction zone initiates along the megathrust, which controls its polarity. The intensity of strain-dependent friction coefficient weakening is crucial for the collapse of shortening and thickening plates and the occurrence of subduction initiation. Without strain-dependent friction coefficient weakening, an elevated symmetrical ridge swelling forms upon forced compression, which is difficult to collapse and initiate the asymmetric subduction system. As for grain damage, it may only play a subordinate role in the near-ridge subduction initiation. In addition, heterogeneous tectonic patterns inheriting from the seafloor spreading have an impact on the formation of near-ridge weak strain localization and subsequent subduction zone geometry. In particular, the uniform subducting slab forms after the symmetric spreading pattern produced at fast spreading ridge. In contrast, the heterogenous and curved subducting slabs are produced after shortening of more heterogeneous (ultra)slow spreading ridges containing both magmatic and amagmatic sections. Opposite subduction polarity induced by inheritance of large offset oceanic transform faults is also

observed in our models. Studies of convergence rates suggest that variable convergence rates can change the rheological coupling conditions which have a great effect on the resulting subduction zone geometry. Comparison of our numerical results with the reconstruction of the Mirdita ophiolite of Albania suggests that the respective subduction zone initiated along the newly formed megathrust rather than along an inherited detachment fault.

Acknowledgments

M.L. would like to acknowledge the support from the China Scholarship Council (201808110216). Open-source Paraview and Matlab software were used to visualize 3D and 2D figures, respectively. Numerical simulations were performed on the ETH-Zurich Euler cluster.

Data Availability Statement

Due to 3D models with very high resolution, output files are too large to be uploaded into the repository. But they can be available from the corresponding author upon request.

Reference

Andreani, M., Escartin, J., Delacour, A., Ildefonse, B., Godard, M., Dyment, J., ... & Fouquet, Y. (2014). Tectonic structure, lithology, and hydrothermal signature of the Rainbow massif (Mid-Atlantic Ridge 36° 14′ N). Geochemistry, Geophysics, Geosystems, 15(9), 3543-3571.

Bach, W., Garrido, C. J., Paulick, H., Harvey, J., & Rosner, M. (2004). Seawater-peridotite interactions: First insights from ODP Leg 209, MAR 15 N. Geochemistry, Geophysics, Geosystems, 5(9).

Beard, James S., B. Ronald Frost, Patricia Fryer, Andrew McCaig, Roger Searle, Benoit Ildefonse, Pavel Zinin, and Shiv K. Sharma. "Onset and progression of serpentinization and magnetite formation in olivine-rich troctolite from IODP Hole U1309D." Journal of Petrology 50, no. 3 (2009): 387-403.

Beaussier, S. J., Gerya, T. V., & Burg, J. P. (2019a). 3D numerical modelling of the Wilson cycle: structural inheritance of alternating subduction polarity. Geological Society, London, Special Publications, 470(1), 439-461.

Beaussier, S. J., Gerya, T. V., & Burg, J. P. (2019b). Near-ridge initiation of intraoceanic subduction: Effects of inheritance in 3D numerical models of the Wilson Cycle. Tectonophysics, 763, 1-13.

Bercovici, D., & Ricard, Y. (2012). Mechanisms for the generation of plate tectonics by two-phase grain-damage and pinning. Physics of the Earth and Planetary Interiors, 202, 27-55.

Bercovici, D., Ricard, Y. (2013). Generation of plate tectonics with two-phase grain-damage and pinning: Source-sink model and toroidal flow. Earth Planet. Sci. Lett. 365, 275–288.

Bercovici, D., & Ricard, Y. (2014). Plate tectonics, damage and inheritance. Nature, 508(7497), 513-516.

Bercovici, D., Schubert, G., Ricard, Y. (2015). Abrupt tectonics and rapid slab detachment with grain damage. Proceed. National Acad. Sci. 112, 1287-1291.

Bercovici, D., & Mulyukova, E. (2021). Evolution and demise of passive margins through grain mixing and damage. Proceedings of the National Academy of Sciences, 118(4).

Bickert, M., Lavier, L., & Cannat, M. (2020). How do detachment faults form at ultraslow mid-ocean ridges in a thick axial lithosphere?. Earth and Planetary Science Letters, 533, 116048.

Bickert, M., Cannat, M., Tommasi, A., Jammes, S., & Lavier, L. (2021). Strain Localization in the Root of Detachment Faults at a Melt-Starved Mid-Ocean Ridge: A Microstructural Study of Abyssal Peridotites From the Southwest Indian Ridge. Geochemistry, Geophysics, Geosystems, 22(5), e2020GC009434.

Boschi, C., Früh-Green, G. L., Delacour, A., Karson, J. A., & Kelley, D. S. (2006). Mass transfer and fluid flow during detachment faulting and development of an oceanic core complex, Atlantis Massif (MAR 30 N). Geochemistry, Geophysics, Geosystems, 7(1).

Boschi, C., Bonatti, E., Ligi, M., Brunelli, D., Cipriani, A., Dallai, L., ... & Bedini, R. M. (2013). Serpentinization of mantle peridotites along an uplifted lithospheric section, Mid Atlantic Ridge at 11 N. Lithos, 178, 3-23.

Bown, J. W., & White, R. S. (1994). Variation with spreading rate of oceanic crustal thickness and geochemistry. Earth and Planetary Science Letters, 121(3-4), 435-449.

Buck, W. R., Lavier, L. L., & Poliakov, A. N. (2005). Modes of faulting at mid-ocean ridges. Nature, 434(7034), 719-723.

Cann, J. R., Blackman, D. K., Smith, D. K., McAllister, E., Janssen, B., Mello, S., & Escartin, J. (1997). Corrugated slip surfaces formed at ridge–transform intersections on the Mid-Atlantic Ridge. Nature, 385(6614), 329.

Clauser, C., Huenges, E. (1995). Thermal conductivity of rocks and minerals. In: Ahrens, T.J. (editor), Rock Physics and Phase Relations. AGU Reference Shelf 3. American Geophysical Union, Washington DC, pp. 105–126.

548 Cloos, M. (1993). Lithospheric buoyancy and collisional orogenesis: Subduction of oceanic plateaus,
549 continental margins, island arcs, spreading ridges, and seamounts. Geological Society of
550 America Bulletin, 105(6), 715-737.
551 Crameri, F., Magni, V., Domeier, M., Shephard, G.E., Chotalia, K., Cooper, G., Eakin, C.M., Grima,
552 A.G., Gürer, D., Király, A., Mulyukova, E., Peters, K., Robert, B., Thielmann, M. (2020) A
553 transdisciplinary and community-driven database to unravel subduction zone initiation. Nature
554 Communications, 11, 1-14.
555 Dick, H. J., Lin, J., & Schouten, H. (2003). An ultraslow-spreading class of ocean
556 ridge. Nature, 426(6965), 405-412.
557 Erickson, S. G. (1993). Sedimentary loading, lithospheric flexure, and subduction initiation at passive
558 margins. Geology, 21(2), 125-128.
559 Escartín, J., Smith, D. K., Cann, J., Schouten, H., Langmuir, C. H., & Escrig, S. (2008). Central role
560 of detachment faults in accretion of slow-spreading oceanic lithosphere. Nature, 455(7214),
561 790-794.
562 Faccenda, M., Gerya, T. V., & Chakraborty, S. (2008). Styles of post-subduction collisional orogeny:
563 Influence of convergence velocity, crustal rheology and radiogenic heat
564 production. Lithos, 103(1-2), 257-287.
565 Forsyth, D., & Uyeda, S. (1975). On the relative importance of the driving forces of plate
566 motion. Geophysical Journal International, 43(1), 163-200.
567 Fujiwara, T., Tamura, C., Nishizawa, A., Fujioka, K., Kobayashi, K., & Iwabuchi, Y. (2000).
568 Morphology and tectonics of the Yap Trench. Marine Geophysical Researches, 21(1), 69-86.
569 Garcés, M., & Gee, J. S. (2007). Paleomagnetic evidence of large footwall rotations associated with
570 low-angle faults at the Mid-Atlantic Ridge. Geology, 35(3), 279-282.
571 Gerya, T. V., & Meilick, F. I. (2011). Geodynamic regimes of subduction under an active margin:
572 effects of rheological weakening by fluids and melts. Journal of Metamorphic Geology, 29(1),
573 7-31.
574 Gerya, T. V. (2013). Three-dimensional thermomechanical modeling of oceanic spreading initiation
575 and evolution. Physics of the Earth and Planetary Interiors, 214, 35-52.
576 Gerya, T. V., Stern, R. J., Baes, M., Sobolev, S. V., & Whattam, S. A. (2015). Plate tectonics on the
577 Earth triggered by plume-induced subduction initiation. Nature, 527(7577), 221-225.
578 Gerya, T. V., Yuen, D. A. (2007). Robust characteristics method for modelling multiphase visco-
579 elasto-plastic thermo-mechanical problems. Physics of the Earth and Planetary Interiors, 163(1-
580 4), 83-105.
581 Gerya, T. V., Bercovici, D., & Becker, T. W. (2021). Dynamic slab segmentation due to brittle–ductile
582 damage in the outer rise. Nature, 599(7884), 245-250.
583 Gregg, P. M., Behn, M. D., Lin, J., & Grove, T. L. (2009). Melt generation, crystallization, and
584 extraction beneath segmented oceanic transform faults. Journal of Geophysical Research: Solid
585 Earth, 114(B11).
586 Gülcher, A. J., Beaussier, S. J., & Gerya, T. V. (2019). On the formation of oceanic detachment faults
587 and their influence on intra-oceanic subduction initiation: 3D thermomechanical
588 modeling. Earth and Planetary Science Letters, 506, 195-208.
589 Gurnis, M., Hall, C., & Lavier, L. (2004). Evolving force balance during incipient
590 subduction. Geochemistry, Geophysics, Geosystems, 5(7).
591 Hilairet, N., B. et al. (2007). High-pressure creep of serpentine, interseismic deformation, and
592 initiation of subduction. Science, 318, 1910–1913.
593 Hirth, G., Kohlstedt, D. (2003). Rheology of the upper mantle and the mantle wedge: a view from the
594 experimentalists. In: Eiler, J. (Ed.), Subduction Factor Monograph, vol.138. American
595 Geophysical Union,Washington, DC, pp. 83–105.
596 Hofmeister, A. M. (1999). Mantle values of thermal conductivity and the geotherm from Phonon

lifetimes. Science, 283, 1699–1706.
Lallemand, S., Arcay, D. (2021) Subduction initiation from the earliest stages to self-sustained subduction: Insights from the analysis of 70 Cenozoic sites. Earth-Science Reviews, 221, 103779.
Liati, A., Gebauer, D., & Fanning, C. M. (2004). The age of ophiolitic rocks of the Hellenides (Vourinos, Pindos, Crete): first U–Pb ion microprobe (SHRIMP) zircon ages. Chemical Geology, 207(3-4), 171-188.
Liu, M., Gerya, T., & Rozel, A. B. (2022). Self-organization of magma supply controls crustal thickness variation and tectonic pattern along melt-poor mid-ocean ridges. Earth and Planetary Science Letters, 584, 117482.
Karato, S., Wu, P. (1993) Rheology of the upper mantle: a synthesis. Science 260, 771–778.
Katz, R. F. (2010). Porosity-driven convection and asymmetry beneath mid-ocean ridges. Geochemistry, Geophysics, Geosystems, 11(11).
Keenan, T. E., Encarnación, J., Buchwaldt, R., Fernandez, D., Mattinson, J., Rasoazanamparany, C., & Luetkemeyer, P. B. (2016). Rapid conversion of an oceanic spreading center to a subduction zone inferred from high-precision geochronology. Proceedings of the National Academy of Sciences, 113(47), E7359-E7366.
Klein, F., Bach, W., Jöns, N., McCollom, T., Moskowitz, B., & Berquó, T. (2009). Iron partitioning and hydrogen generation during serpentinization of abyssal peridotites from 15 N on the Mid-Atlantic Ridge. Geochimica et Cosmochimica Acta, 73(22), 6868-6893.
MacLeod, C. J., Escartin, J., Banerji, D., Banks, G. J., Gleeson, M., Irving, D. H. B., ... & Smith, D. K. (2002). Direct geological evidence for oceanic detachment faulting: The Mid-Atlantic Ridge, 15 45′ N. Geology, 30(10), 879-882.
MacLeod, C. J., Carlut, J., Escartín, J., Horen, H., & Morris, A. (2011). Quantitative constraint on footwall rotations at the 15° 45′ N oceanic core complex, Mid-Atlantic Ridge: Implications for oceanic detachment fault processes. Geochemistry, Geophysics, Geosystems, 12(5).
Maffione, M., Morris, A., & Anderson, M. W. (2013). Recognizing detachment-mode seafloor spreading in the deep geological past. Scientific reports, 3(1), 1-6.
Maffione, M., Morris, A., Plümper, O., & van Hinsbergen, D. J. (2014). Magnetic properties of variably serpentinized peridotites and their implication for the evolution of oceanic core complexes. Geochemistry, Geophysics, Geosystems, 15(4), 923-944.
Maffione, M., Thieulot, C., Van Hinsbergen, D. J., Morris, A., Plümper, O., & Spakman, W. (2015). Dynamics of intraoceanic subduction initiation: 1. Oceanic detachment fault inversion and the formation of supra-subduction zone ophiolites. Geochemistry, Geophysics, Geosystems, 16(6), 1753-1770.
Mével, C. (2003). Serpentinization of abyssal peridotites at mid-ocean ridges. Comptes Rendus Geoscience, 335(10-11), 825-852.
Montési, L. G., Behn, M. D., Hebert, L. B., Lin, J., & Barry, J. L. (2011). Controls on melt migration and extraction at the ultraslow Southwest Indian Ridge 10–16 E. Journal of Geophysical Research: Solid Earth, 116(B10).
Morgan, J. P., & Ghen, Y. J. (1993). Dependence of ridge-axis morphology on magma supply and spreading rate. Nature, 364(6439), 706-708.
Morris, A., Gee, J. S., Pressling, N., John, B. E., MacLeod, C. J., Grimes, C. B., & Searle, R. C. (2009). Footwall rotation in an oceanic core complex quantified using reoriented Integrated Ocean Drilling Program core samples. Earth and Planetary Science Letters, 287(1-2), 217-228.
Mulyukova, E., Bercovici, D. (2017). Formation of lithospheric shear zones: Effect of temperature on two-phase grain damage. Phys. Earth Planet. Inter. 270, 195–212.
Plümper, O., Røyne, A., Magrasó, A., & Jamtveit, B. (2012). The interface-scale mechanism of reaction-induced fracturing during serpentinization. Geology, 40(12), 1103-1106.

646 Plümper, O., Beinlich, A., Bach, W., Janots, E., & Austrheim, H. (2014). Garnets within geode-like
647 serpentinite veins: Implications for element transport, hydrogen production and life-supporting
648 environment formation. Geochimica et Cosmochimica Acta, 141, 454-471.
649 Qing, J., Liao, J., Li, L., & Gao, R. (2021). Dynamic evolution of induced subduction through the
650 inversion of spreading ridges. Journal of Geophysical Research: Solid Earth, 126(3),
651 e2020JB020965.
652 Olive, J. A., Behn, M. D., & Tucholke, B. E. (2010). The structure of oceanic core complexes
653 controlled by the depth distribution of magma emplacement. Nature Geoscience, 3(7), 491-495.
654 Ranalli, G. Rheology of the Earth (Chapman and Hall, 1995).
655 Regenauer-Lieb, K., Yuen, D. A., & Branlund, J. (2001). The initiation of subduction: criticality by
656 addition of water?. Science, 294(5542), 578-580.
657 Rozel, A. B., Ricard, Y., & Bercovici, D. (2011). A thermodynamically self-consistent damage
658 equation for grain size evolution during dynamic recrystallization. Geophysical Journal
659 International, 184(2), 719–728.
660 Sauter, D., Cannat, M., Rouméjon, S., Andreani, M., Birot, D., Bronner, A., ... & MacLeod, C. J.
661 (2013). Continuous exhumation of mantle-derived rocks at the Southwest Indian Ridge for 11
662 million years. Nature Geoscience, 6(4), 314.
663 Schierjott, J. C., Thielmann, M., Rozel, A. B., Golabek, G. J., Gerya, T. V. (2020). Can Grain Size
664 Reduction Initiate Transform Faults? —Insights From a 3-D Numerical study. Tectonics, 39(10),
665 e2019TC005793.
666 Schroeder, T., John, B., & Frost, B. R. (2002). Geologic implications of seawater circulation through
667 peridotite exposed at slow-spreading mid-ocean ridges. Geology, 30(4), 367-370.
668 Smith, D. K., Escartín, J., Schouten, H., & Cann, J. R. (2008). Fault rotation and core complex
669 formation: Significant processes in seafloor formation at slow-spreading mid-ocean ridges (Mid-
670 Atlantic Ridge, 13–15 N). Geochemistry, Geophysics, Geosystems, 9(3).
671 Spray, J. G. (1983). Lithosphere–asthenosphere decoupling at spreading centers and initiation of
672 obduction. Nature, 304(5923), 253-255.
673 Stern, R. J., & Bloomer, S. H. (1992). Subduction zone infancy: examples from the Eocene Izu-
674 Bonin-Mariana and Jurassic California arcs. Geological Society of America Bulletin, 104(12),
675 1621-1636.
676 Stern, R. J. (2004). Subduction initiation: spontaneous and induced. Earth and Planetary Science
677 Letters, 226(3-4), 275-292.
678 Stern, R. J., & Gerya, T. (2018). Subduction initiation in nature and models: A
679 review. Tectonophysics, 746, 173-198.
680 Theissen-Krah, S., Iyer, K., Rüpke, L. H., & Morgan, J. P. (2011). Coupled mechanical and
681 hydrothermal modeling of crustal accretion at intermediate to fast spreading ridges. Earth and
682 Planetary Science Letters, 311(3-4), 275-286.
683 Torsvik, T. H., Van der Voo, R., Preeden, U., Mac Niocaill, C., Steinberger, B., Doubrovine, P. V., ...
684 & Cocks, L. R. M. (2012). Phanerozoic polar wander, palaeogeography and dynamics. Earth-
685 Science Reviews, 114(3-4), 325-368.
686 Tucholke, B. E., Behn, M. D., Buck, W. R., & Lin, J. (2008). Role of melt supply in oceanic
687 detachment faulting and formation of megamullions. Geology, 36(6), 455-458.
688 Turcotte, D. L. & Schubert, G. Geodynamics (Cambridge Univ. Press, 2002).
689 Whitney, D. L., Teyssier, C., Rey, P., & Buck, W. R. (2013). Continental and oceanic core
690 complexes. Bulletin, 125(3-4), 273-298.

691 **Table 1. Results of numerical experiments.** Sp: spreading rate; Conv, convergence rate; Trant: transition time from divergence to convergence; SW:
692 strain weakening; GSE: grain size evolution; lDF: long detachment faults; sDF: short detachment faults; sNF: symmetric normal faults; HF: horse faults; Mag:
693 magmatic segments; aMag; amagmatic segments; FZ, narrow fracture zones; Tranf: transform faults; Oblir: oblique ridge; Strar: straight ridge; SI: subduction
694 initiation. *, reversal models.

Model	Sp (*mm/yr*)	Different from reference model	Spreading pattern	Inversion results
fIm3	10	Reference	lDF, Mag, aMag, FZ, Oblir	Near ridge SI in same direction, subduction modes controlled by aMag
v50	5	Sp: 5 mm/yr, Trant: 30-31 Myr	lDF, sparse Mag, aMag, Strar	Near ridge SI in same direction, subduction modes controlled by aMag
v75	7.5	Sp: 7.5 mm/yr, Trant: 20-22 Myr	lDF, Mag, aMag, Oblir	Near ridge SI in same direction, subduction modes controlled by aMag
2fg	20	Sp: 20 mm/yr, Trant: 7-10 Myr	sDF, lDF, Tranf, Oblir	Near ridge SI in opposite directions, subduction modes controlled by Tranf
4fg	40	Sp: 40 mm/yr, Trant: 4-6 Myr	sNF, sDF, Strar	Near ridge SI in same direction
8fg	80	Sp: 80 mm/yr, Trant: 2-3 Myr	sNF, Strar	Near ridge SI in same direction
tm100	10	Low bottom temperature (-100 K)	sDF, lDF, sparse Mag, aMag	Near ridge SI in opposite directions, subduction modes controlled by Tranf and aMag
tp100	10	High bottom temperature (+100 K)	lDF, Tranf, thick crust, Strar	Near ridge SI in opposite directions, subduction modes controlled by Tranf
nwn00	10	No SW in crust and mantle	sDF, HF, Mag, aMag, Strar	Failed SI, two active conjugate thrusts on both side of former spreading ridges
rhng	10	No GSE	lDF, Mag, aMag, FZ, Tranf, Oblir	Near ridge SI in opposite directions, subduction modes controlled by Tranf and aMag
e33w63	10	Moderate SW in the crust and mantle	sDF, HF, Mag, aMag, Strar	Part SI, two active conjugate thrusts on both side of former spreading ridges
n33w63	10	Moderate SW in the crust and mantle, no GSE	sDF, HF, Mag, aMag, Strar	Part SI, two active conjugate thrusts on both side of former spreading ridges
n33w66	10	No SW in crust and mantle, no GSE	sDF, HF, Mag, aMag, Strar	Failed SI, two active conjugate thrusts on both side of former spreading ridges
c33w66	10	No SW in crust	lDF in aMag, sDF and HF in Mag, Strar	Near ridge SI in opposite directions, subduction modes controlled by aMag
ob11	10	Oblique ridge: 19°, Trant: 12-15 Myr	lDF, Mag, aMag, Oblir	Near ridge SI in same direction, subduction modes controlled by aMag
ob22	10	Oblique ridge: 38°, Trant: 10-12 Myr	lDF, Mag, aMag, Oblir	Near ridge SI in opposite directions, subduction modes controlled by aMag
av1	left - 5	Asymmetric Sp and Conv, Trant:	lDF, Tranf, Mag, aMag, Oblir	Near ridge SI in opposite directions, subduction

	right - 10	8.5-9.5 Myr		modes controlled by Tranf and aMag
av2	left - 10 right - 5	Asymmetric Sp and Conv, Trant: 8.5-9.5 Myr	lDF, Mag, aMag, Strar	Near ridge SI in same direction, subduction modes controlled by aMag
contl*	-	Conv: left-10 mm/yr, right-0 mm/yr	Same with reference model	Same with reference model except for the trench position
contr*	-	Conv: left-0 mm/yr, right-10 mm/yr	Same with reference model	Same with reference model except for the trench position
rheo1*	-	Conv: 10 mm/yr	lDF, Mag, aMag, FZ, Oblir	Near ridge SI in same direction, subduction modes controlled by aMag
rheo2*	-	Conv: 20 mm/yr	Same with rheo1*	Near ridge SI in opposite directions, subduction modes controlled by aMag
rheo4*	-	Conv: 40 mm/yr	Same with rheo1*	Same with rheo2*

695